Article:
Shi, L, Yu, Z and Jaworski, AJ (2010) Application of laser-based instrumentation for measurement of time-resolved temperature and velocity fields in the thermoacoustic system. International Journal of Thermal Sciences, 49 (9). 1688 - 1701. ISSN: 1290-0729

https://doi.org/10.1016/j.ijthermalsci.2010.03.015

Application of laser-based instrumentation for measurement of time-resolved temperature and velocity fields in the thermoacoustic system

Lei SHI, Zhibin YU and Artur J. JAWORSKI *

School of Mechanical, Aerospace and Civil Engineering,

University of Manchester, Sackville Street, PO Box 88, Manchester, M60 1QD,

United Kingdom

ABSTRACT:

This work aims to develop reliable laser-based measurement techniques to enable fundamental heat transfer and fluid flow studies in thermoacoustic systems. The challenge is to better understand the modes of energy transfer between the key components, such as stacks (or regenerators) and the hot and cold heat exchangers (located on two sides of the stack/regenerator structure), under the oscillatory flow conditions imposed by the acoustic field. The measurement methodologies adopted in this work include combined two-dimensional temperature and velocity field measurements using Planar Laser Induced Fluorescence (PLIF) and Particle Image Velocimetry (PIV), respectively. These are investigated around the fins of a pair of mock-up heat exchangers placed side by side in a quarter wavelength standing wave acoustic resonator, to mimic the working conditions of a thermoacoustic system. The fins are kept at constant temperatures by means of resistive heating and water cooling, respectively. The velocity and temperature field distributions for 20 phases in the acoustic cycle have been obtained. The impact of the inertial, viscous and thermal effects on the time-dependent local temperature and velocity distributions is discussed. Mutual interaction between both fields is also shown. Future work towards obtaining useful heat transfer correlations in oscillatory conditions is outlined.

* Corresponding author; e-mail a.jaworski@manchester.ac.uk, tel. +44(0)1612754352, fax. +44(0)7053604497

1. Introduction and background

Thermoacoustic engines and refrigerators rely on a thermal interaction between an oscillatory compressible flow and solid structures such as thermoacoustic stacks (regenerators) and heat exchangers. The role of these solid structures is to either produce acoustic power, due to an imposed temperature gradient, or to produce a refrigeration (heat pumping) effect, induced by an acoustic excitation. These heat transfer processes are based on the so called "thermoacoustic effect" where appropriately phased pressure and velocity oscillations enable the compressible fluid to undergo a thermodynamic cycle in the vicinity of a solid body [1,2].

Figure 1 shows a schematic of one possible implementation of a standing wave thermoacoustic engine. Here, the temperature gradient along a stack of parallel plates, forming a series of parallel channels, is imposed by two heat exchangers, hot and cold, located at the stack's extremities. When the thermoacoustic onset conditions are met, a spontaneous acoustic wave is generated. As indicated by the inset at the bottom, on the micro-scale of the individual fluid elements located in the stack channels, the acoustic wave induces a hydrodynamic energy transfer cascade, whereby oscillating fluid elements, undergoing cyclic compression and expansion processes, transfer heat from the hot to the cold end of the stack. In this example, the acoustic power is extracted by a linear alternator to generate electricity. Other configurations may include thermoacoustic coolers or heat pumps coupled to the engine, while the engine's topology may be altered to a travelling wave configuration, both of these aspects being omitted here.

In the macro-scale, Figure 1 shows the main heat flux streams between the device and its surroundings, as well as the internal heat transfer streams on the interfaces between the stack and heat exchangers. Of course the white arrows only symbolize the net time averaged heat fluxes, while in reality the heat transfer phenomena are governed by the physics of the oscillatory flow. One of the main difficulties in designing thermoacoustic devices from the viewpoint of thermal performance is the lack of any reliable heat transfer correlations for the oscillatory flow conditions. Typically, it is assumed that the length of the heat exchangers should simply be equal to the displacement amplitude of the fluid particle, while the heat

transfer rates are predicted using typical engineering handbook correlations, strictly developed for steady flows. There is clearly a need for experimental investigations into the heat transfer rates in the oscillatory flows and subsequently developing the relevant heat transfer correlations for the actual conditions found in the thermoacoustic devices.

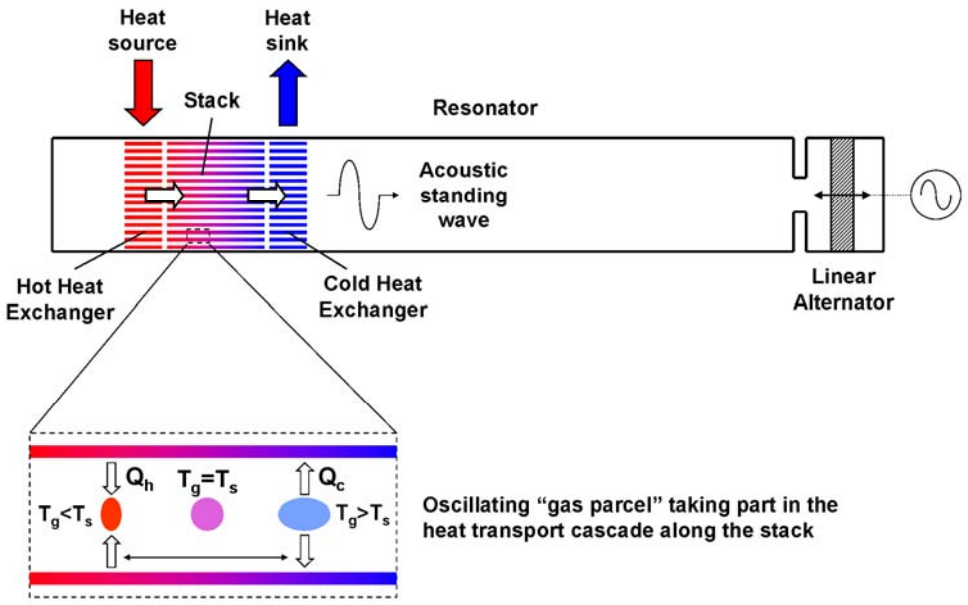

Figure 1 General schematic of the overall heat fluxes in a standing wave thermoacoustic engine.

Turning to the flow in the vicinity of the stack and heat exchanger interface, it needs to be realised that the interaction of the acoustic field with the solid boundary results in complex fluid flow and heat transfer processes, which are not fully understood, especially for large acoustic excitations. Very complex flow patterns occur due to the cross-sectional discontinuities at the end of stack and heat exchanger [3], which give rise to complicated vortex shedding or channel "entrance effects". Inevitably these lead to local pressure losses, increasing the energy dissipation in the system, but also most likely lead to the modification of the local heat transfer rates, compared to steady-flow conditions, which makes the steady flow calculations questionable.

Therefore, this work is driven by the need for a better understanding of the fluid flow and heat transfer processes, in particular the quantitative description of the heat transfer rates in the heat exchangers and

stacks. On the one hand, these processes are one of the bottlenecks for achieving higher thermodynamic efficiencies of the current thermoacoustic devices. On the other hand, the performance of heat exchangers in the oscillatory flow is difficult to predict, as most of the available handbook data relate to steady flows, while the experimental studies are very limited.

It is thought that one of the possible ways of obtaining reliable heat transfer information are detailed quantitative measurements of spatially and temporally resolved temperature and velocity fields around the internal structures of thermoacoustic devices. Therefore, the objective of this work is to develop and demonstrate the appropriate experimental techniques to include Planar Laser Induced Fluorescence (PLIF) and Particle Image Velocimetry (PIV) to enable detailed studies of heat transfer and fluid flow processes taking place on the micro-scale of the oscillatory flow around the solid surfaces that form the main components of the thermoacoustic devices. This kind of data can potentially be used to obtain both local and global (as well as instantaneous and/or cycle-averaged) heat transfer rates, which could be used for devising new heat transfer correlations. Similarly, such data would be useful for validation of future CFD codes that could be used for predicting the performance of thermoacoustic systems.

2. Literature review

This section reviews state-of-the-art of the present methods, that can be used for thermal and flow field studies within thermoacoustic systems – in particular those capable of obtaining temperature and velocity fields. For clarity, the following sub-sections contain material divided into thermal and velocimetry methods, respectively.

2.1. Thermal measurements in thermoacoustic systems

Most commonly, heat transfer measurements within oscillatory flows, and thermoacoustic systems in particular, include time-averaged methods such as thermocouples embedded within the internal solid structures. For example, Leong and Jin [4, 5] and Jin and Leong [6] developed an experimental apparatus to investigate heat transfer rates into the channel walls due to an oscillatory flow. Here the oscillating

flow was induced by a piston-cylinder arrangement. Aluminium foam was investigated as a means of enhancing fluid-to-wall heat transfer rates. Comparisons between steady and oscillatory flows were made and it was shown that in the latter the averaged Nusselt number was significantly enhanced. Conceptually, this arrangement is similar to investigating heat transfer rates within thermoacoustic stacks, regenerators and heat exchangers. Gopinath and Harder [7] used thermocouples to investigate the convective heat transfer behaviour from a cylinder in an intense acoustic field which is representative of a strong zero-mean oscillatory flow. The cylinder could be representative of a heat exchanger tube while the oscillatory acoustically induced flow can represent the flow conditions in a thermoacoustic engine. They developed correlations between Nusselt and Reynolds numbers for the heat transfer from a cylinder in a low-amplitude oscillatory flow.

Within thermoacoustic context, Paek et al. [8] and Nsofor et al. [9] reported the experimental study of heat transfer in the oscillatory flow at the heat exchangers of thermoacoustic systems. They also used thermocouples to measure the temperatures at the heat exchangers, and obtained their heat transfer correlations in terms of Nusselt, Prandtl and Reynolds numbers. In general terms, heat transfer studies such as these provide measurements of the average heat transfer rates obtained from an energy balance approach. They are capable of providing global correlations, where various geometrical parameters of flow conditions can be factored in by studying a large number of experimental cases – but provide very little insight into the interdependencies between the actual flow conditions and the heat transfer phenomena.

A somewhat different approach, aiming at establishing time-resolved temperature field distributions within the working fluid of thermoacoustic systems relies on the application of the cold-wire anemometry. Here a standard “hot-wire” probe, driven in a constant current mode can be used to measure high frequency temperature signal. By locating such probes in selected locations and traversing them across the thermal boundary layers in the vicinity of the surfaces taking part in the heat exchange processes one could in principle establish local heat transfer rates, or subsequently time-dependent Nusselt numbers. Measurements of this kind have been performed by Huelsz and Ramos [10], who obtained oscillating temperature and the relative phase between temperature and pressure oscillations in

acoustic waves. Mao and Jaworski [11] also conducted similar cold-wire measurements of a thermal boundary layer in a channel of parallel-plate thermoacoustic stack. However the usefulness of such methods is questionable: the probes are usually intrusive and perturb the flow significantly. In addition they only provide "point-wise" measurements: covering a substantial heat transfer area with sufficient spatial resolution is extremely time-consuming and access to some areas of stacks or heat exchangers would be very challenging.

In the class of full temperature field measurement methods, applied to investigations of fluid temperature field in thermoacoustics, Wetzel and Herman [12-14] carried out pioneering work in using holographic interferometry combined with high-speed cinematography to visualize the full temperature fields at the edge of a single stack plate located in an acoustic standing-wave. They demonstrated the difference between heat transfer in oscillatory flows with zero mean velocity and steady flows. They also managed to document the complex heat transfer mechanisms between fluid and solid material at the end of a stack plate arising from the thermoacoustic effect. From the measurement point of view, a novel evaluation procedure that accounts for the influence of the acoustic pressure variations on the refractive index was applied to accurately reconstruct the high-speed, two-dimensional oscillating temperature distributions. Nevertheless, it seems that the complexity of the method developed limits its wider application.

2.2. Velocity measurement in thermoacoustic systems

The three main techniques for velocity measurements in thermoacoustic context include: Hot Wire Anemometry (HWA), Laser Doppler Anemometry (LDA) and Particle Image Velocimetry (PIV). The principles of applying single hot-wire probes to measure velocity fluctuations in the thermoacoustic resonator have been presented by Huelsz and Lopez-Alquicira [15] in the same physical arrangement as described in [10]. Of course, it is well known that a single hot-wire probe is insensitive to flow direction and so additional methods need to be in place for defining the actual phase of the velocity signal. In addition, hot- wire measurement suffers from the same shortcoming as already mentioned cold-wire methods: in order to cover a large flow region, the probe must be traversed through possibly thousands of locations, which is very cumbersome, especially in tight spaces between stack or heat exchanger plates.

However, there are some clear advantages of hot wire methods in thermoacoustics. Firstly, the flow requires no seeding, which simplifies the experimental apparatus. Secondly, HWA offers relatively high temporal resolution of the acquired signal. For example, in the already mentioned work by Mao et al. [3] hot wire anemometry was used to detect velocity fluctuations related to vortex shedding phenomena behind thermoacoustic stacks, which allowed obtaining reliable Strouhal number characteristics. Thirdly, the typical wire diameter of hot-wire probe is of the order of 5 μm, which can potentially deliver high spatial resolution if fine stepper motor controls can be deployed (about an order of magnitude better than the LDA and PIV methods discussed below). An example of the application of HWA in a thermoacoustic stack is discussed by Mao et al. [16].

Bailliet et al. [17] proposed to use combination of LDA measurement of the acoustic velocity and the microphone-based acoustic pressure measurement. They demonstrated the experimental determination of the possible working frequencies of thermoacoustic refrigerator; that is the frequencies that provide the maximum acoustic power flow at the resonator entrance. Similarly, it was shown that it is possible to measure acoustic power flow along the resonator with a good spatial resolution. Thompson et al. [18] showed the application of LDA to investigate the influence of a thermoacoustically induced axial temperature gradient and of fluid inertia on the acoustic streaming induced in a cylindrical standing-wave resonator. Evidently, the LDA methods were not used for measuring the acoustic velocity in tight spaces of internal structures of thermoacoustic devices. This is most likely due to practical difficulties of introducing convergent laser beams. Another disadvantage of LDA is relatively poor spatial resolution: the typical dimensions of the measurement spot are around 50 μm.

Applications of PIV for flow visualization or velocity measurement in acoustic systems were reported by Hann and Greated [19,20] who used a double exposure on a single frame and an auto-correlation method. Campbell et al. [21] carried out a review of PIV (as well as LDA) methods in sound measurement applications, and focused in particular on measurements illustrating streaming effects in acoustic systems using PIV. More recent work by Nabavi et al. [22] focused on simultaneous measurement of acoustic and streaming velocities at selected phases of the acoustic cycle , the former obtained by cross-correlating two consecutive PIV images, while the latter was obtained by cross-correlating the alternative PIV images at

the same phase. A good agreement between experiments and theoretical predictions was reported. A somewhat similar approach was adopted by Debesse et al. [23] who measured acoustic and streaming velocities in a high pressure (7 – 15 bar) standing wave resonator working with nitrogen at a frequency of 22 Hz. Here the acoustic excitation was induced by a thermoacoustic engine located at one end of the resonator, while the velocity fields were measured at the other end, through a short cylindrical section made out of glass.

The flow field around internal structures of thermoacoustic systems was perhaps first investigated by Blanc-Benon et al. [24]. They used a quarter-wavelength thermoacoustic refrigerator configuration, driven by a loudspeaker at a frequency of 200 Hz. The experiments were conducted for two stacks: one with plate thickness of 0.15 mm and plate spacing of 1.0 mm, the other with plate thickness of 1.0 mm and plate spacing of 2.0 mm. The drive ratios were relatively low: 1.5% and 1.0%, respectively. The measurements were locked onto the loudspeaker signal. Vortex structures around the edges of stack plates were obtained by averaging of 100 PIV images taken at selected phases of the acoustic cycle (altogether 16 phases in an acoustic cycle were investigated). The results showed both concentrated and elongated eddies, which nevertheless remained attached to the plates. Further investigations of velocity fields generated by the oscillatory flow past the parallel-plate stacks were carried out by Castrejón-Pita et al. [25], Mao et al. [26] Berson and Blanc-Benon [27], Berson et al. [28], Aben et al. [29] and Jaworski et al [30]. Generally speaking**,** all these works focused on velocity and vorticity fields in order to classify the flow morphology as a function of stack geometries and acoustic excitation levels. Some similarity criteria have also been suggested to find the controlling parameters for this type of flow.

3. Measurement techniques and experimental setup

As is clear from the above literature review, the velocity field measurement using PIV is relatively well established in the thermoacoustic context. Also, the principles of PIV operation are usually well known, and so they will not be repeated in this paper. However, there are only a limited number of previous studies which allow imaging of the temperature field. The holographic interferometry technique discussed earlier seems relatively complicated for practical thermoacoustic applications. An ideal candidate would

be a technique that could use as many common components with a PIV system as possible, which would allow a common experimental setup. Planar laser-induced fluorescence (PLIF) is such an attractive non-intrusive and quantitative temperature imaging method that is often offered as an add-on to commercially available PIV systems. It can provide full temperature field information over the imaging area, which could be of benefit to spatially and temporally resolved heat transfer studies, and could potentially address many of the measurement challenges of the thermoacoustic systems. Furthermore, a combined use of PIV and PLIF has already been described by Bresson et al. [31], which provides a good starting point for extending this approach to thermoacoustic systems. The molecular tracer chosen for current PLIF measurements is acetone vapour. The following three sub-sections will explain briefly the principles of acetone-based PLIF measurement; describe the experimental apparatus; and discus the implementation of PIV and PLIF in the current setup, respectively.

3.1. Principles of acetone PLIF

In a typical acetone PLIF experiment, the flow is illuminated by a UV laser sheet, which is tuned to excite a particular transition of an acetone molecular tracer. A fraction of the molecules in the appropriate ground state absorbs the incident light and is promoted to the first excited singlet state. Some of the excited molecules may dissociate. The rest returns to the equilibrium state either by emitting photons or by transferring the excess of energy through non-radiative decay processes (collisional quenching, intersystem crossing or internal conversion). The photons can be spontaneously emitted on short time scales and fluorescence occurs [32]. For "weak" excitation (i.e. non-saturating), the fluorescence signal S_f, in number of photons collected, is given [33,34] as:

$$S_f = \frac{E}{hc/\lambda}\eta_{opt} dV_c \left[\frac{\chi_{acetone} P}{kT}\right] \sigma(\lambda, T)\phi(\lambda, T, P, \sum_i \chi_i) \qquad (1)$$

In equation (1), E is the laser fluence [J/cm^2], hc/λ is the energy [J] of a photon at the excitation wavelength λ, η_{opt} is the overall efficiency of the collection optics, and dV_c is the collection volume [cm^3]. The bracketed term is the acetone number density [cm^{-3}], given as the product of mole fraction

$\chi_{acetone}$ and total pressure P divided by the Boltzmann constant k times temperature T. The final two quantities are σ, the molecular absorption cross-section of the tracer [cm^2], and ϕ, the fluorescence quantum yield.

For gas-phase PLIF measurement, acetone is an effective seeding compound due to a number of attractive features [31]: it possesses a broadband absorption spectrum extending from 225 to 320 nm, which can be easily excited by conventional high power UV lasers; depending on the excitation wavelength, the broadband fluorescence located between the 350-550 nm wavelength range exhibits a highly versatile sensitivity to temperature; its molecule has a very high vapour saturation pressure; it has low toxicity and low cost. Acetone PLIF has been widely used for gas-phase scalar mixing studies [32,35], turbulent jet flow studies [31,36], and gas-phase free convection flow studies [37].

In a given experiment, the collection optics, the collection volume and the laser excitation wavelength are constant. The pressure dependence of PLIF signals on the excitation wavelength of 266 nm is 5% per MPa [38]. Even at large acoustic excitation such as pressure amplitude of 10,000 Pa, the PLIF signal maximum oscillation is only 0.05%. Thus, the pressure dependence of PLIF signals can be neglected in the current experimental conditions where the pressure amplitude reaches only 500 Pa. Therefore, at the conditions of constant mole fraction of acetone, the fluorescence signal can be expressed as only a function of temperature:

$$S_f \propto \frac{1}{T}\sigma(T)\phi(T)\,. \tag{2}$$

3.2. Description of experimental apparatus

The experimental apparatus used in the current study is shown schematically in Figure 2. Its main part is a 7.4 m long resonator made out of several sections of metal tube of square cross-section, with internal dimensions 134 mm x 134 mm. One of the sections is a 2.3 m long test section, made out of aluminium and equipped with a number of windows to allow laser illumination and imaging. The remaining sections

are made out of mild steel. One end of the resonator (to the left of Figure 2a) is closed by an "end-cap". The other end is connected to a relatively large "loudspeaker box" (600 x 600 x 600 mm) through a 0.3 m long pyramidal section to match the change in cross-sectional dimensions. Figure 2a shows the overall dimensions of the rig, while Figure 2b is a close up photograph of the test section.

The acoustic excitation which generates an acoustic standing wave inside the resonator is provided by an 18 inch diameter loudspeaker (Model PD1850 rated at 600W). The loudspeaker is driven by an acoustic audio amplifier (made by Void Acoustics, model Network 4) while the sinusoidal signal fed into the amplifier comes from a digital signal generator TTi-TG1010A. By changing the amplitude of this signal, one can control the acoustic excitation and thus the acoustic drive ratio in the rig (i.e. the ratio of the maximum pressure amplitude to the mean pressure in the resonator). The detailed theoretical and experimental analysis of the acoustic coupling between the loudspeaker and the resonator was carried out by Marx et al. [39]. It was shown that the rig operates in quarter-wavelength mode at the frequency of 13.1 Hz. A microphone (Brüel & Kjær Model 4136) is flush-mounted within the "end-cap" to measure the pressure amplitude at the resonator's pressure anti-node, in order to control the acoustic excitation level (the drive ratio). The maximum drive ratio that can be obtained in the rig is of the order of 10%, although in the current studies only drive ratios of up to 0.5% were used to match the acoustic displacement to the heat exchanger length. The instantaneous pressure measured by the microphone is also used as a reference signal to trigger the PIV and PLIF imaging, phase locked to the acoustic cycle.

For PIV studies, the resonator is normally filled with air at atmospheric pressure and room temperature. For PLIF studies the working gas can be either air or nitrogen, with added acetone vapour. The choice depends on whether the selected acetone concentration leads to a flammability hazard within the air-acetone vapour mixture. In the current work, the acetone vapour concentration was only 2%, which allowed safe rig operation with air. For the sake of separating the gas containing acetone vapour from the sensitive components of the excitation loudspeaker, a 0.25 mm thick latex membrane was introduced between the loudspeaker box and the pyramidal section. Because of the relatively small drive ratios used in the experiments no harmful non-linear acoustic effects were observed due to the presence of the membrane.

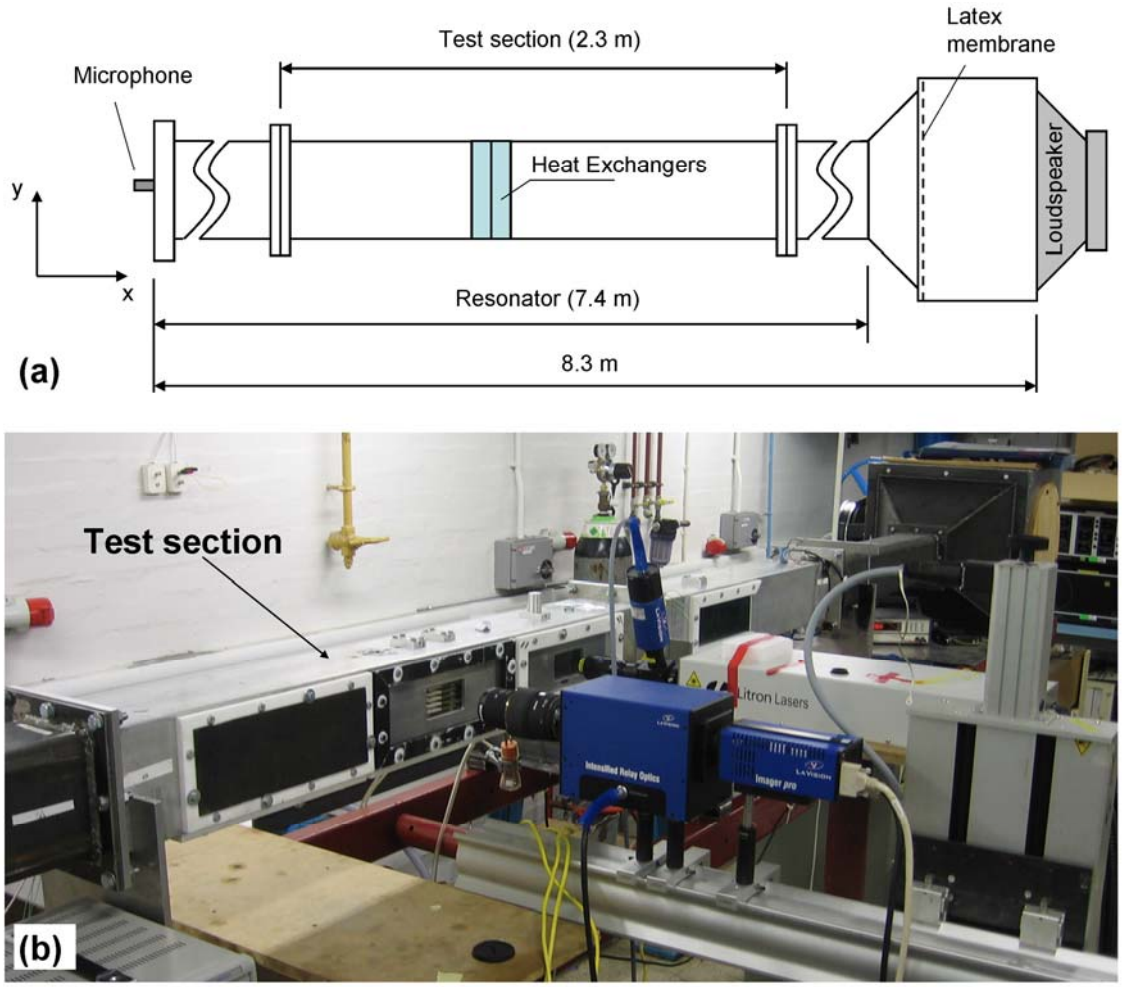

Figure 2 Schematic of the experimental apparatus (a) and a close-up of the test section (b).

The main objective of the work described here was to prove the methodology of combined temperature and velocity field measurement. Therefore the physical arrangement on which the heat transfer and fluid flow processes could be studied was greatly simplified compared to real thermoacoustic devices. In particular, to avoid a complicated laser illumination and to improve the temperature contrast for the PLIF measurements, only a pair of "mock-up" heat exchangers is studied. Furthermore, they are placed side by side to eliminate the need of illuminating the gap between their fins. The fluid flow and heat transfer processes are studied just in one selected channel of such a heat exchanger "pair". This configuration is realistic to some extent for the class of "stack-less" thermoacoustic devices [40,41], however no gap between hot and cold heat exchangers is not, because in reality it would lead to a conductive heat leakage. However, this aspect was not considered important in the current study. It should also be added that from

the point of view of the classification of thermoacoustic devices, the experimental arrangement is strictly neither an “engine” nor a “cooler”. Although a temperature gradient is imposed, it is too small to induce acoustic self-excitation. Thus, in order to provide a mechanism for oscillatory heat transfer, an external acoustic excitation (loudspeaker) has to be applied. Therefore, one could look at the experimental device as an engine-like configuration where the lack of critical temperature gradient is overcome by an external excitation.

Figure 3a shows schematically the experimental arrangement of heat exchangers, with analogous heat flux arrows as those shown in Figure 1. Figure 3b shows the actual implementation within the resonator. Hatched area in Figure 3a indicates the PIV and PLIF imaging area. The laser sheet is introduced from the right. The heat exchanger assembly is placed within the test section (cf. Figure 2b), 4.6 meters (about 0.17 of the wavelength) from the end cap of the resonator.

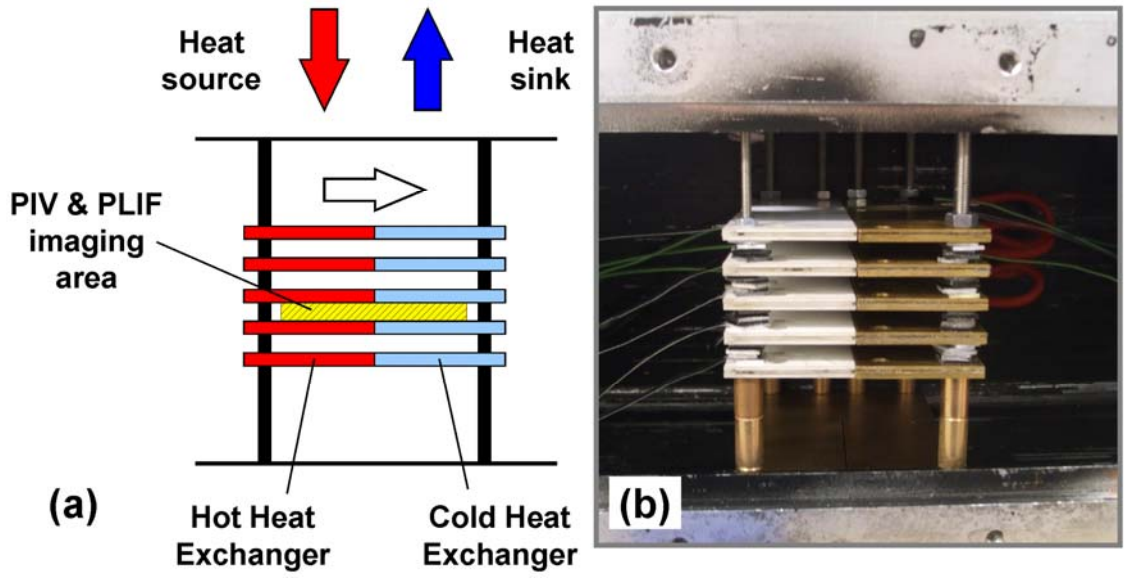

Figure 3 Schematic of the heat exchanger configuration (a), and the photograph of the physical implementation (b).

Both the hot and cold heat exchangers have five fins. Each hot heat exchanger fin is made of a pair of ceramic plates with a resistance heating ribbon sandwiched between them. The cold heat exchanger fins

are made of two brass plates, in one of which a meandering channel is made for water circulation. Both the ceramic fins with ribbon heaters and the brass water-cooled fins are bonded together with a silicone adhesive sealant. The length, l_h, of both types of fins is 35mm, while their width is 132mm (length refers to the flow direction, while width to the span-wise direction). The fin thickness (d_h) and the gap between fins (D_h) of both the hot and cold heat exchangers are kept the same: 3.2 mm and 6.0 mm, respectively. The heat exchangers are equipped with three standard K-type thermocouples; two are used to monitor the surface temperature of the hot and cold fins, while the third one is used for reference temperature measurement within gas needed during the PLIF calibration procedure.

The particular choice of the plate dimensions and gap between fins (spacing) was a trade-off between various practical considerations. On the one hand, the plates need to contain the heating and cooling elements and it was thought that that approximately 3 mm thickness was about right as a starting point in developing hardware (in future manufacture of thinner plates may be feasible, perhaps around 1.5mm). On the other hand, having fixed the plate thickness, the other two remaining considerations were the flow blockage ratio and the ratio of plate spacing to the thermal penetration depth which is one of the design parameters in thermoacoustic systems (ideally between 2 – 4). The choice of 6 mm spacing seemed a reasonable choice: the blockage ratio is around 70%, while the ratio of plate spacing to thermal penetration depth is in the range 5 – 8 (depending on the local gas temperature). In future implementations, as the plate are designed thinner, they could be brought closer together thus improving the latter ratio. The scale of the flow is also congruent with the current collection aperture of PLIF system, which allows for an optimum signal-to-noise ratio in the current setup.

As explained above, the flow velocity amplitude and thus the corresponding Reynolds number can be controlled by varying the excitation of the loudspeaker. The velocity amplitude (u) in the hot and cold heat exchangers can be estimated from PIV. In the experiments described here the highest velocity amplitude, u, used is 2.4 m/s. Thus, the Reynolds number based on the thickness of the fin ($\mathrm{Re}=ud_h/\nu$) and the displacement amplitude of gas particle ($\xi=u/\omega$, where ω is the oscillation angular frequency) are calculated as 480 and 28 mm, respectively. The local Reynolds number ($A=2u/(\nu\omega)^{0.5}$) is used to determine the flow regime according to the criterion by Merkli and Thomann [42]. The calculated local

Reynolds number is around 130, which is much less than the critical Reynolds number 400 and indicates a laminar flow regime. It is also worth noting that Womersley number ($Wo=D_h/(2\nu/\omega)^{0.5}$) in the current setup is in the range 6.2 – 9.6 and according to Kurzweg et al. [43] transition would not occur as long as Reynolds number is kept below the critical value. The DC power supply provides 240W of electrical power to the hot heat exchanger fins at this flow condition. When reaching a steady-state (the indications of thermocouples placed on the surface of hot and cold heat exchangers do not change for half an hour), the hot heat exchanger fins reach the temperature of around 200°C, while the fins of the cold heat exchanger are kept at the temperature of 30°C by the circulating water. Generally the choice of the temperature difference between the hot and cold heat exchangers in the experiments reported here was dictated by two opposing factors. On the one hand, the adhesives used in the construction of the hot plate could only operate up to about 200-220°C, without leading to loss of structural integrity. On the other hand, the accuracy and resolution of PLIF methods improves as the temperature range increases. Operating the hot plates at around 200°C seemed a reasonable choice from the practical point of view.

3.3. Description of the laser-based measurement setup

Figures 4 and 5 show schematically the implementation of the PIV and PLIF systems within the experimental apparatus described above, respectively. It is worth pointing out that the velocity and temperature fields are not measured simultaneously, but the separate measurements repeated at the same operating conditions. Truly simultaneous measurement would simply be impractical as the two techniques require different seeding (oil droplets vs. acetone vapour). Similarly, because the velocity and temperature fields are obtained by averaging a large number of images obtained for the same phase in the acoustic cycle, there is little benefit in obtaining the individual images simultaneously. However, technically such possibilities exist provided an additional camera is available.

PIV System

Flow field measurements were performed using a PIV system by LaVision as shown in Figure 4. The laser sheet is generated by a dual Nd:YAG laser with a wavelength of 532 nm, and combined with sheet

optics and divergence lens. It enters the resonator perpendicularly to its axis, is reflected by a 25 mm diameter mirror and becomes parallel to the resonator axis and normal to the surface of the heat exchanger fins. The distance between the mirror and the heat exchangers is around 300 mm (an order of magnitude more than the maximum gas displacement amplitude); no discernible effect of the mirror on the flow around heat exchangers has been detected during the preliminary tests. Images are taken by LaVision Imager Pro plus camera with a 4 mega-pixel CCD sensor and post processed using commercial software LaVision DaVis 7.2. The flow is seeded with olive oil droplets, produced by an oil droplet generator (TSI's model 9307). The mean droplet diameter is 1 μm. Cross-correlation mode is used and the interrogation window is 16 pixels by 16 pixels. The field of view of the PIV images is 53 mm x 53 mm – in practice this means that the useful image of the inside of the channel is 6 mm x 53 mm. At this field of view the spatial resolution of velocity vector field is 0.41 mm, however in certain experiments a "zoomed-in" view of 15 mm x 15 mm was used to improve the velocity field resolution within the boundary layer.

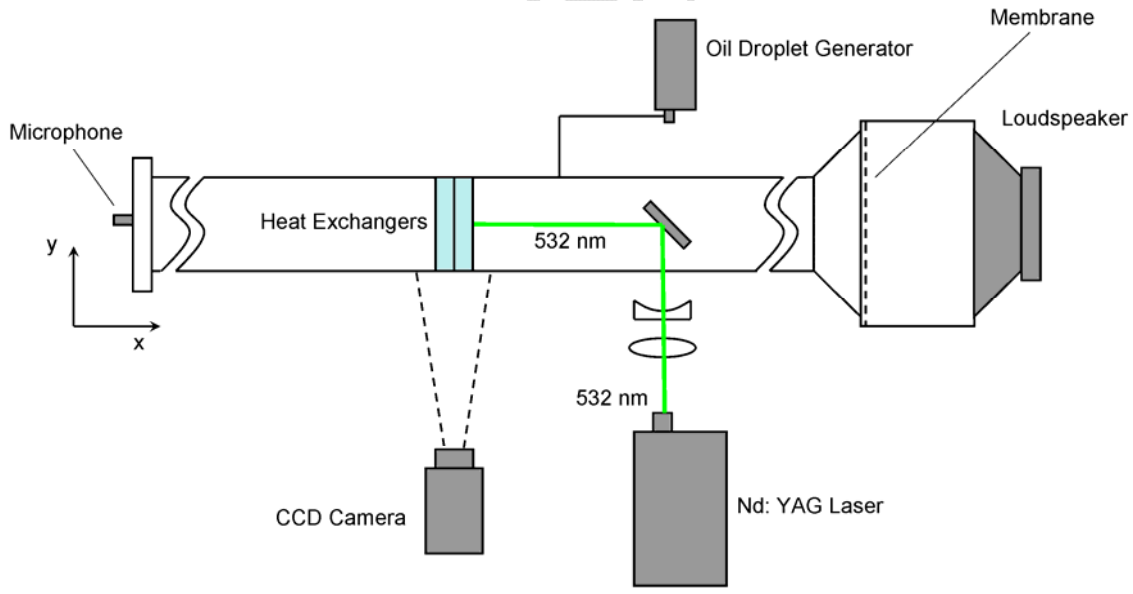

Figure 4 Schematic of the PIV setup.

The time separation between two laser pulses needs to vary according to the velocity magnitude at the selected phase, in order to meet the criterion that the displacement of the seeding particles between two

pictures should be as large as possible but should not exceed one quarter of the interrogation window [44]. The time separation in the phases where velocity reaches its amplitude is 80 microseconds. The accuracy of PIV measurement was validated at the condition of an empty resonator without heat exchangers, where theoretical velocity can be easily predicted from the pressure amplitude measurement using the linear acoustic model [45]. The acoustic velocity in a cycle measured by PIV was compared with the velocity calculated based on the theoretical prediction, and the maximum relative error has been less than 3.6%. Another estimate was obtained by calculating the average velocity value based on 100 measurements together with the standard deviation of instantaneous velocities from the average. Standard deviation has always been less than 2% [46].

PLIF System

PLIF system used in the current study is an extension of the PIV system by LaVision described above. As shown in Figure 5, the laser beam with a wavelength of 532 nm passes a nonlinear crystal and becomes a UV beam of a wavelength of 266 nm. The UV laser sheet is also generated by combining sheet optics with a divergence lens. An energy monitor mounted in front of sheet optics is used to correct laser energy variations because the PLIF signal is sensitive to laser energy variations. The UV laser sheet illuminates the heat exchanger fins through the same light path as PIV (cf. Figure 4). Image detection system consists of LaVision Imager Pro Plus camera with a 4 mega-pixel CCD sensor, Intensified Relay Optics (IRO), band pass filter for PLIF of radical and UV lens. IRO is an electronic shutter device with a widely variable exposure time, which is placed in front of the camera for an increased sensitivity, as well as an increased gain and gating capability. The 2 x 2 hardware “binning” in the camera setup is used for increasing the ratio of PLIF signal to noise. Here, “binning” specifies the collection of a certain number of pixels to a “super pixel”. Thus, the effective resolution of the CCD sensor is reduced to 1024 pixels x 1024 pixels. Images are post processed using LaVision DaVis 7.2 with PLIF software extension. The field of view of the PLIF images is also 53 mm x 53 mm, corresponding to the spatial resolution of 19.3 pixels per 1 mm.

The oil droplet generator used in PIV is replaced by a rather more complicated seeding system of acetone-based PLIF shown in Figure 5. Before performing the PLIF experiments, the resonator needs to be seeded with acetone vapour of specified concentration (in the present measurements 2%). The detailed operation of the acetone seeding system is explained by Shi et al. [47]. It is worth noting that in planning the experiments care has been taken to limit the exposure of acetone vapour to no more than 10,000 laser shots, as preliminary analysis indicated that in the current configuration and for the laser power used this would not lead to any discernible loss of fluorescence due to acetone photo-dissociation (see for example [34]). The detailed analysis of PLIF measurement uncertainty can be found elsewhere [48].Based on the ensemble averaging of 200 instantaneous images the relative temperature measurement error when using absolute temperature scale is between 3.1 and 3.4% in the range between 20 and 200°C

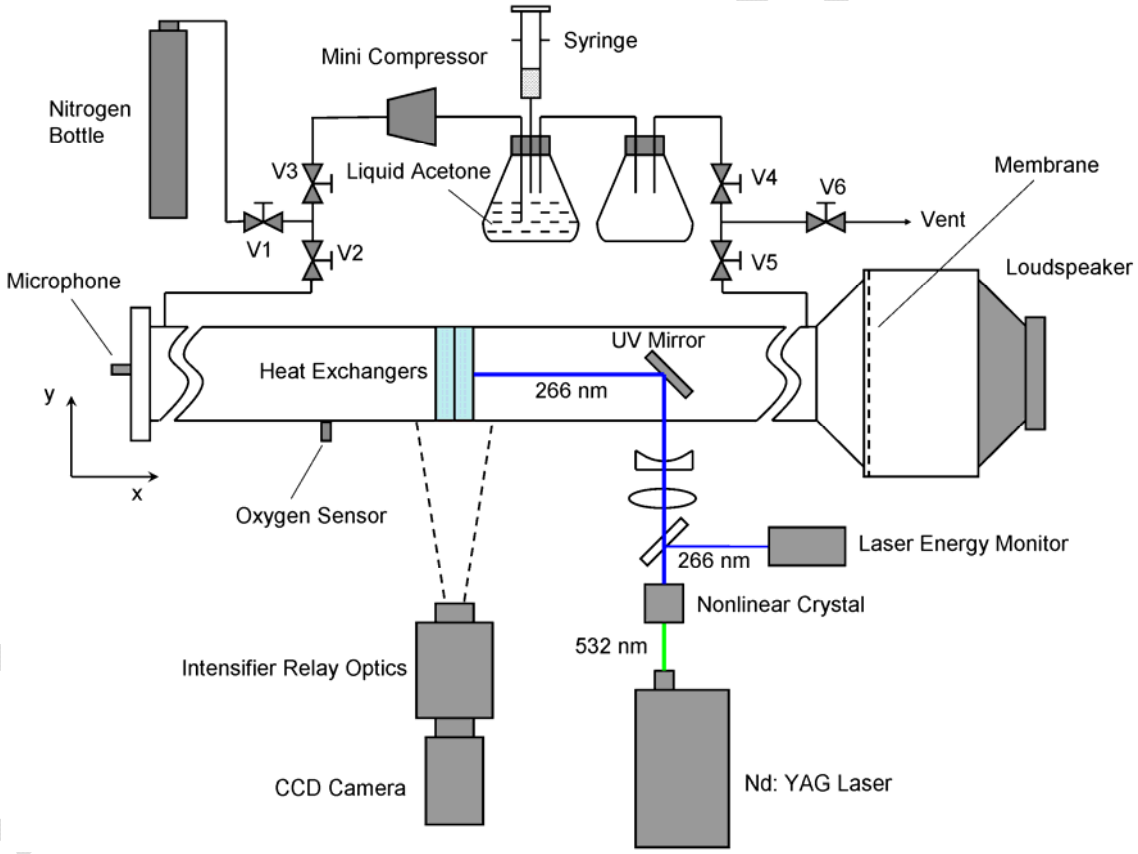

Figure 5 Schematic of the PLIF setup.

In practice, in order to obtain temperature data, a number of system calibration steps need to be followed. These include: background subtraction, sheet image correction, energy correction and temperature

calibration, which are described in some detail by Shi et al. [47]. Temperature calibration is carried out before each experimental run, after the rig has been filled with acetone vapour. During calibration (performed in the absence of acoustic excitation) a thermocouple is exposed to hot gas in the vicinity of the hot heat exchanger, while at the same time the fluorescence intensity signal is recorded from the image pixel immediately adjacent to the thermocouple. Between the time the resistive heating is switched on and the time the heat exchanger plate reaches the final temperature, it is possible to cover the full temperature measurement range of about 20 – 200°C. An example of a calibration curve is shown in Figure 6 – the exponential fitting coefficients shown in the graph are used by the imaging software.

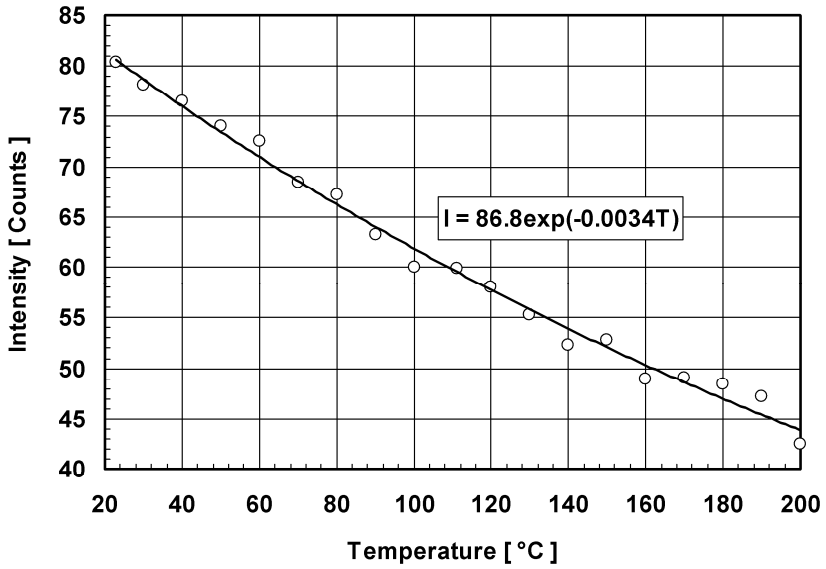

Figure 6 Sample PLIF temperature calibration.

Phase locking of laser measurements

Both the velocity and temperature field measurements were performed for 20 phases in an acoustic cycle as illustrated in Figure 7 (for the drive ratio of 0.3%), which shows the reference pressure signal at the end of the resonator measured by the microphone, the reference velocity signal at the hot/cold heat exchanger location, measured by PIV and the calculated reference displacement at the hot/cold exchanger location. The directions of the velocity and displacement are according to the coordinate system shown in Figure 2. The phase locking system is described in more detail in reference [3]. For each phase, 100 pairs

of frames were taken to calculate the phase-averaged velocity, while 200 LIF images were taken for phase-averaged temperature fields. The increase of the number of frames and images beyond 100 and 200, respectively, provides negligible accuracy gains in terms of the resulting velocity and temperature fields.

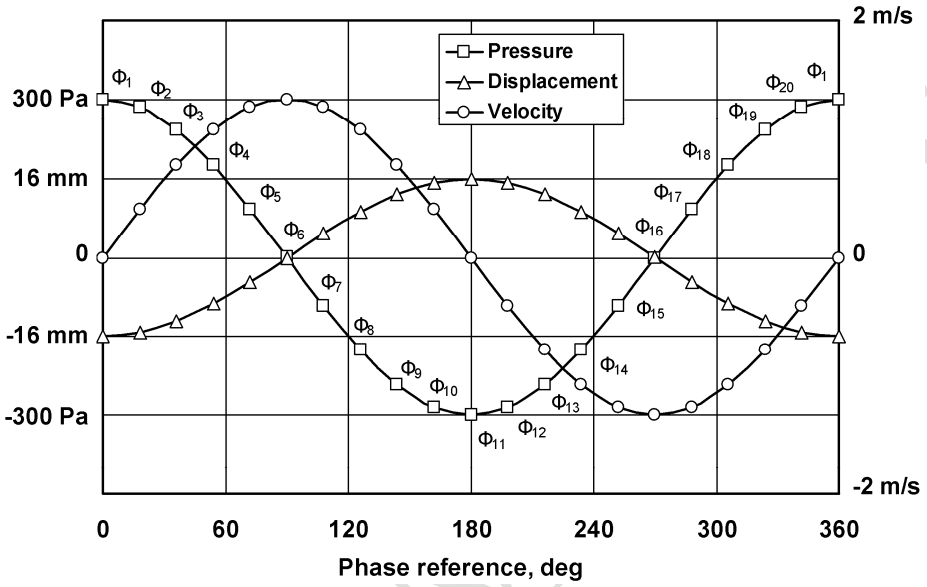

Figure 7 Reference pressure, displacement and velocity signal for 20 phases interrogated in an acoustic cycle. Drive ratio is 0.3%.

4. Sample experimental results and discussion

As described in Section 3.3, the temperature and velocity field measurements were performed for 20 phases in an acoustic cycle. In this paper, six phases are selected to represent the characteristic flow and heat transfer features of the whole cycle. Figure 8 shows the temperature field and axial velocity distribution in a few cross-sections along the heat exchanger for phases: Φ_1, Φ_4, Φ_7, Φ_{10}, Φ_{15} and Φ_{19} (cf. also Figure 7) obtained for the drive ratio of 0.3% (fluid displacement amplitude $\xi = 16$ mm at the heat exchanger location). To help the interpretation of results, an elliptical shape marks a hypothetical fluid element and its displacement from its "equilibrium position" located at the plane where hot and cold heat exchangers join.

At phase Φ_1 (Figure 8a), the fluid displacement reaches the maximum positive value, which means that the gas parcel in the channel moves farthest to the left. At this phase, the cross-sectional mean velocity of fluid is zero (see Figure 7). From the velocity field, it can be seen that the velocity near the wall is negative while the velocity remains in the positive direction at the centre of the channel. This is due to the inertial effects from the previous half cycle. It can be seen that, at this instant the cold gas penetrates far into the channel of the hot heat exchanger (referred as hot channel thereafter). The gas is heated by the plates. After this phase, the gas parcel starts to accelerate to move to the right.

Figure 8b shows the temperature and velocity distributions at phase Φ_4. It can be found that, there exists a velocity overshoot in the velocity distribution – the maximum axial velocity occurs near the wall rather than at the centre of the channel. The occurrence of the velocity overshoot is due to the combined effects of the axial pressure gradient, viscous and inertial effects. At the centre of the channel, the flow is controlled only by the axial pressure gradient and inertial force since it is so far from the wall that the viscous effects can be ignored. Near the wall, the viscous effect plays such a significant role that it causes the phase lead in the near wall flow over the core flow in the axial pressure gradient [45]. From the temperature image, it can be found that the cold gas partly flows out from the hot channel after being heated. The hot gas takes over the left end of the hot channel.

At phase Φ_7 (Figure 8c), the fluid has just passes the velocity peak at Φ_6, and starts to decelerate. The gas parcel passes the equilibrium and goes into the channel between the cold plates (referred to as the cold channel thereafter). The velocity overshoot becomes less pronounced. In Figure 8c, it can be seen that the hot gas occupies most of the hot channel. However, the central area at the right of the hot channel still shows relatively low temperatures. This indicates that during the preceding quarter cycle ($\Phi_1 - \Phi_6$) the heat transfer from the hot plate to the gas has not influenced the gas temperature in the central area significantly.

At phase Φ_{10} (Figure 8d), it can be seen that the hot gas gradually penetrates into the cold channel. The velocity overshoot near to the wall disappears because of the inertial effect of gas in the central area of the channel and viscous effect of the gas near to the wall. The velocity profiles exhibit a parabola-like shape.

It is also found that the velocity boundary layer thickness is increasing from the right to the left of the channel. This is because the gas viscosity increases with the increase of the temperature. From the temperature field, it can be found that the hot channel is occupied by the hot gas and the cold channel remains at low temperature.

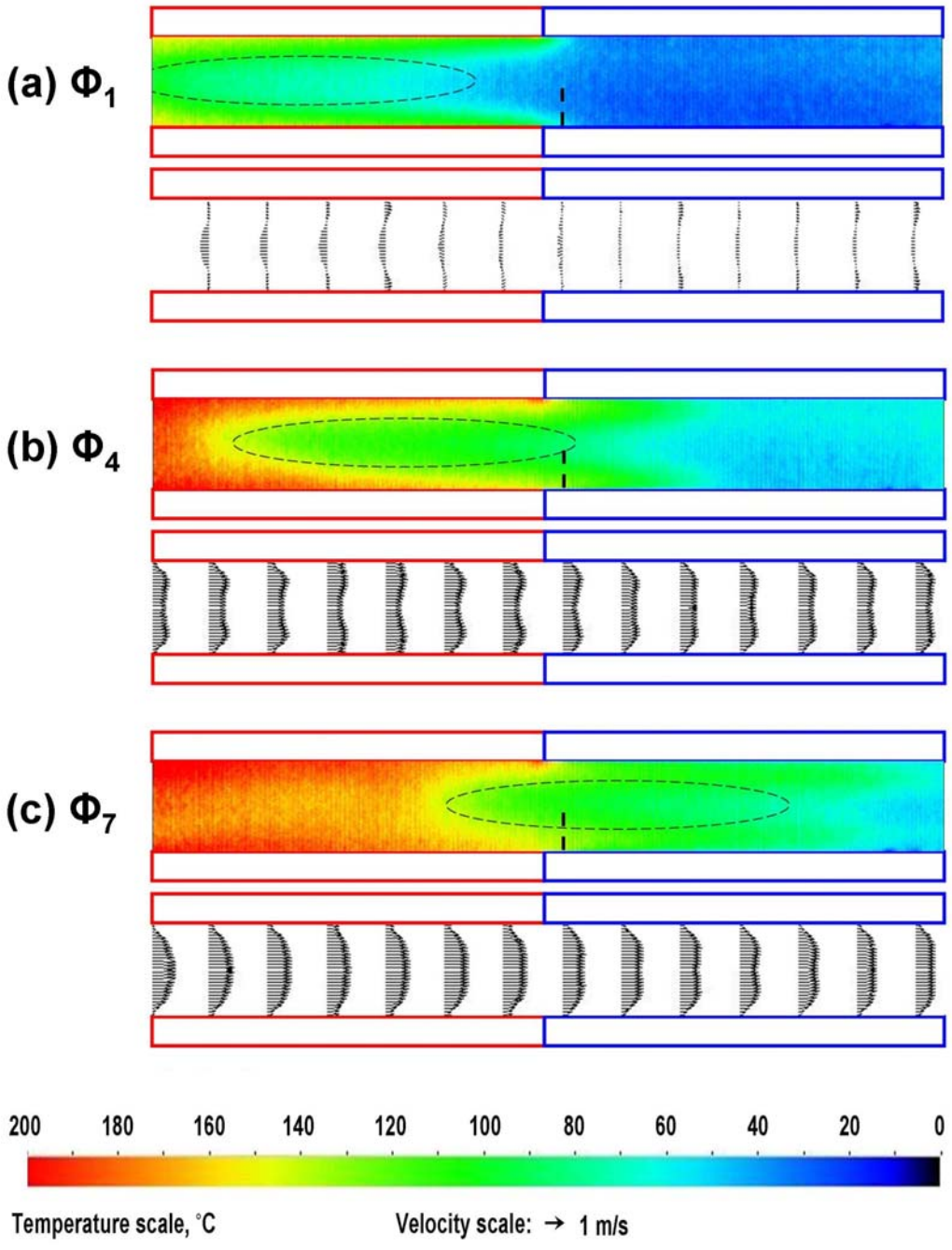

Figure 8 Temperature and velocity distributions for six selected phases in an acoustic cycle at drive ratio of 0.3%. Only one channel is shown, the viewing area being 6 x 53 mm. Red rectangles mark the heated plates, while blue rectangles mark the cooled plates in the heat exchanger assembly.

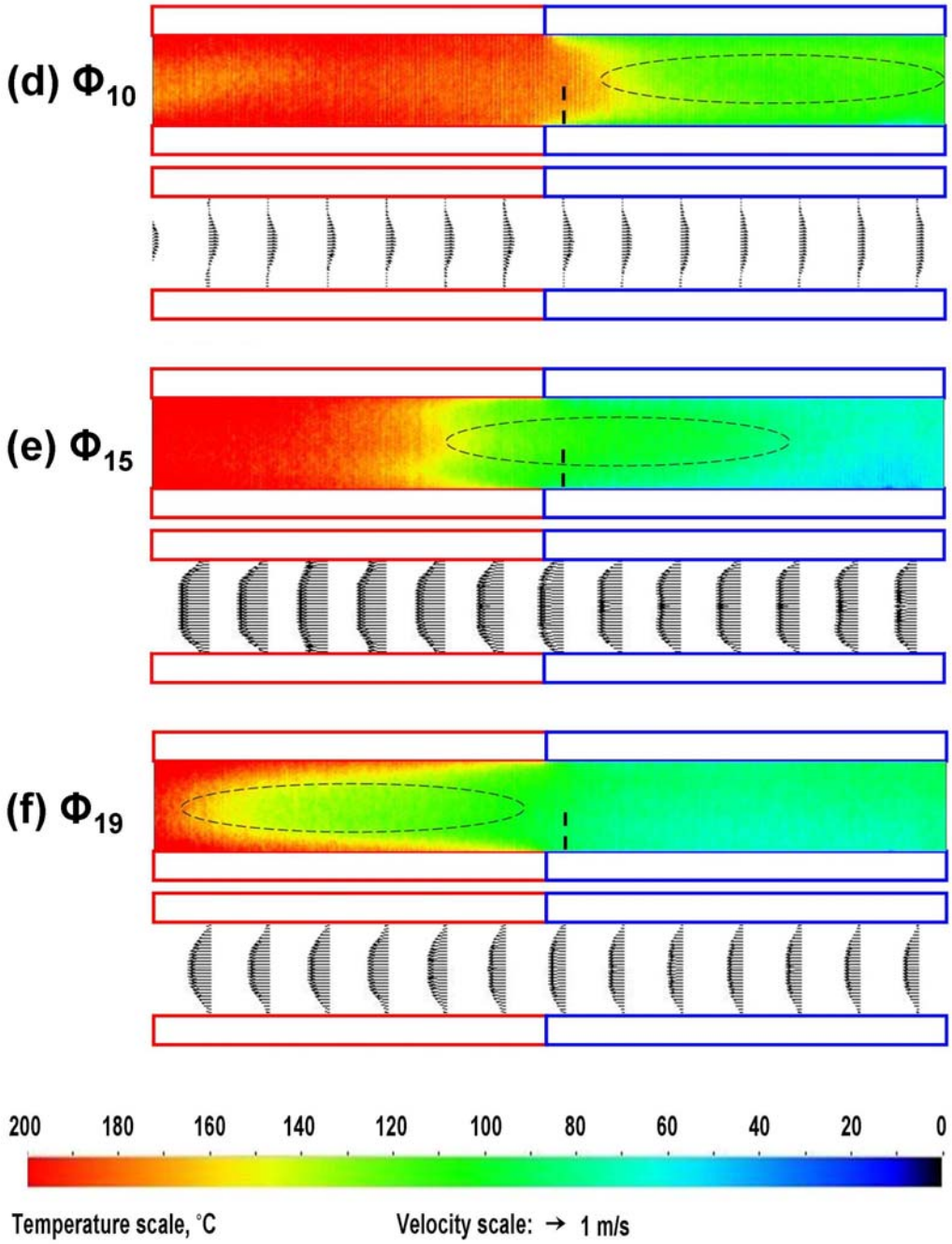

Figure 8 (*continued*) Temperature and velocity distributions for six selected phases in an acoustic cycle at drive ratio of 0.3%. Only one channel is shown, the viewing area being 6 x 53 mm. Red rectangles mark the heated plates, while blue rectangles mark the cooled plates in the heat exchanger assembly.

In Figure 8e (phase Φ_{15}), the displacement is close to zero and the velocity is close to its positive peak (cf. Figure 7). It can be seen that the velocity field looks somewhat similar to that at phase Φ_7, but the direction is reversed. From the temperature field distribution, the gas temperature is relatively low at the right end of the hot channel, compared with the hot gas at the left end. This is because, between phase Φ_6 and Φ_{16}, this part of gas is in the cold channel, and its thermal energy has been partly transferred to the cold plates. Figure 8e also illustrates very well an interesting feature of the velocity profiles: the bulk velocity has a larger magnitude in the hot channel than in the cold channel. This is congruent with the change of gas density with temperature. A similar behaviour is also shown in Figure 9e obtained for the higher drive ratio.

Figure 8f (phase Φ_{19}), the cold gas penetrates deep into the hot channel. The velocity decreases and assumes a value consistent with the next cycle. The change of the velocity profiles indicates the change in the boundary layer thickness along the x-direction from right to left.

It should be noted that in Figure 8 the velocity profiles are obtained for the camera view of 53 mm x 53 mm (i.e. to cover the full channel view of 6 mm x 53 mm). Such a resolution is insufficient to capture the flow within the viscous boundary layer. This can be seen on the profiles as "slipping" velocities in certain cross-sections of the channel. To eliminate this problem, the velocity field needs to be investigated at higher resolution using for example 15 mm x 15 mm camera view. Indeed this increased resolution is sufficient to capture the velocity profiles as shown in Figure 10 discussed below. However, Figure 8 is useful for identifying the overall flow features in the whole length of the channel.

It is also interesting to see that in Fig. 8e (phase Φ_{15}) the temperature profile taken a few millimetres to the left of the "joint" between hot and cold plates exhibits an interesting "temperature undershoot" pattern (cf. the area where red, green and yellow colours are plotted closely together). Here the temperature seems high at the wall (red colour), drops down within the boundary layer (green colour) and raises again closer to the channel centre (yellow and red colours). It is worth noting that such temperature behaviour can also be seen in the preceding phases $\Phi_{11} - \Phi_{14}$ which are omitted to save space. The mechanism causing the "temperature undershoot" will be discussed in detail later in this paper.

Figure 9 shows temperature and velocity field data analogous to Figure 8, but at a higher drive ratio of 0.5% (fluid displacement amplitude ξ = 28 mm at the heat exchanger location). Clearly, at the higher amplitude the hypothetical fluid element, marked again by a dashed ellipse, is displaced outside the field of view for some parts of the cycle (cf. phase Φ_1 and Φ_{10}, for example). Importantly, however for such a high displacement the whole length of the cold channel is exposed to the hot fluid that arrived from the hot side (cf. Figure 9d), which will engage a higher proportion of the fin length in the fluid-to-solid heat transfer. Conversely, as seen from Figure 9a, a higher proportion of the hot fins can interact with the cold fluid arriving from the hot channel.

For further analysis of fluid flow and heat transfer processes, the cross sectional temperature profile in the hot and cold channel can be investigated at a selected stream-wise locations. Here, as an example the attention will be focussed on the selected cross section in the cold channel, 2 mm away from the "joint" between the hot and cold heat exchangers, which is indicated by the vertical dashed lines marked in Figures 8 and 9. Figure 10 shows the corresponding temperature profiles (top) and velocity profiles (bottom) obtained for the selected cross section at the drive ratio of 0.5%, for the six phases discussed with reference to Figures 8 and 9. The distance from the wall used for plotting the temperature and velocity profiles is normalized by the channel width, D_h = 6 mm. Normalised fluid temperature is expressed as

$$\theta = \frac{T_f - T_w}{T_H - T_C} \tag{3}$$

where θ, T_f, T_w, T_H and T_C are the normalised fluid temperature, local fluid temperature, local wall (fin) temperature, reference hot temperature (here 200ºC), and reference cold temperature (here 30ºC), respectively. Normalised velocity is expressed as

$$u^*(x,y,t) = u(x,y,t)/u \tag{4}$$

where u is simply the oscillating velocity amplitude, introduced in Section 3.2.

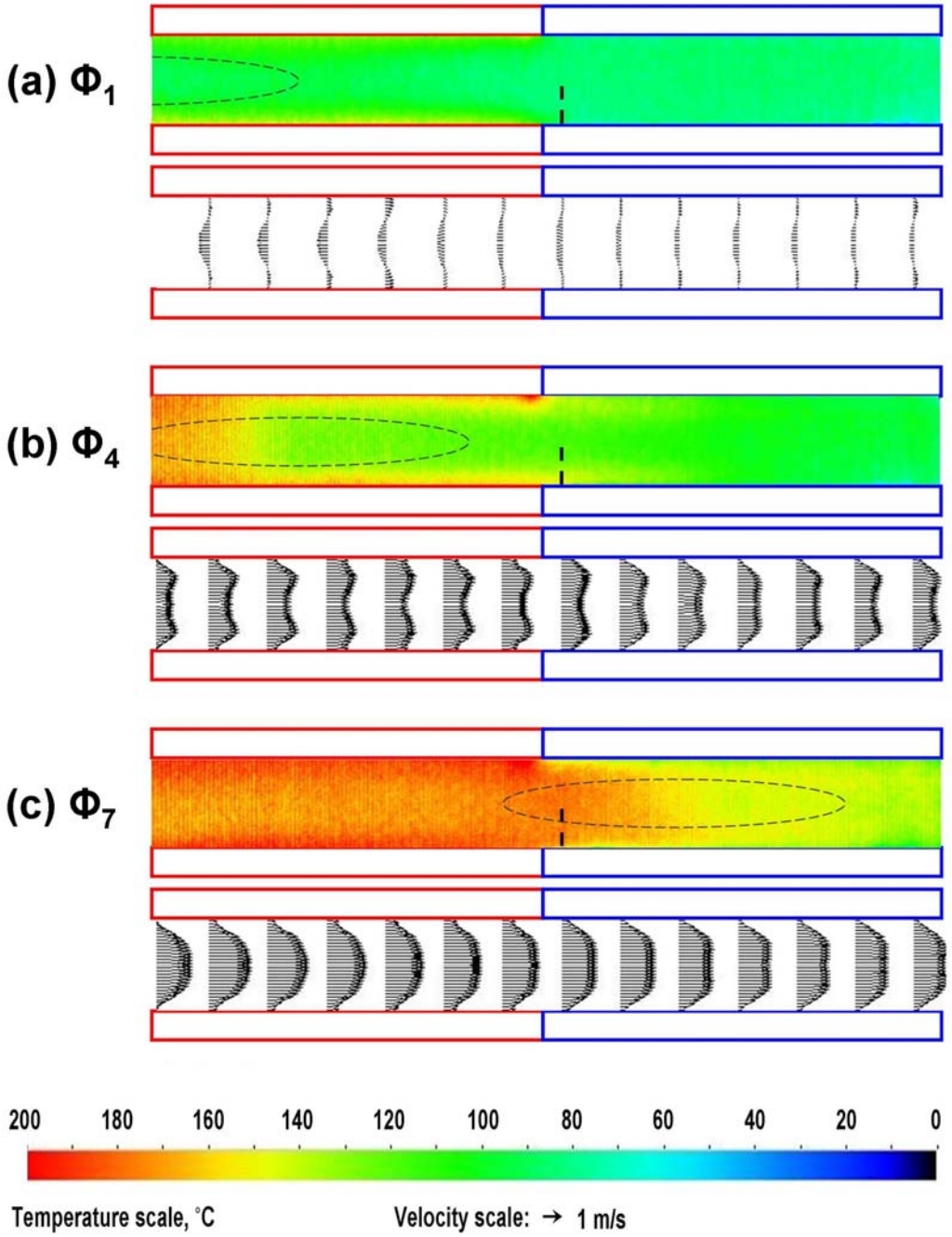

Figure 9 Temperature and velocity distributions for six selected phases in an acoustic cycle at drive ratio of 0.5%. Only one channel is shown, the viewing area being 6 x 53 mm. Red rectangles mark the heated plates, while blue rectangles mark the cooled plates in the heat exchanger assembly.

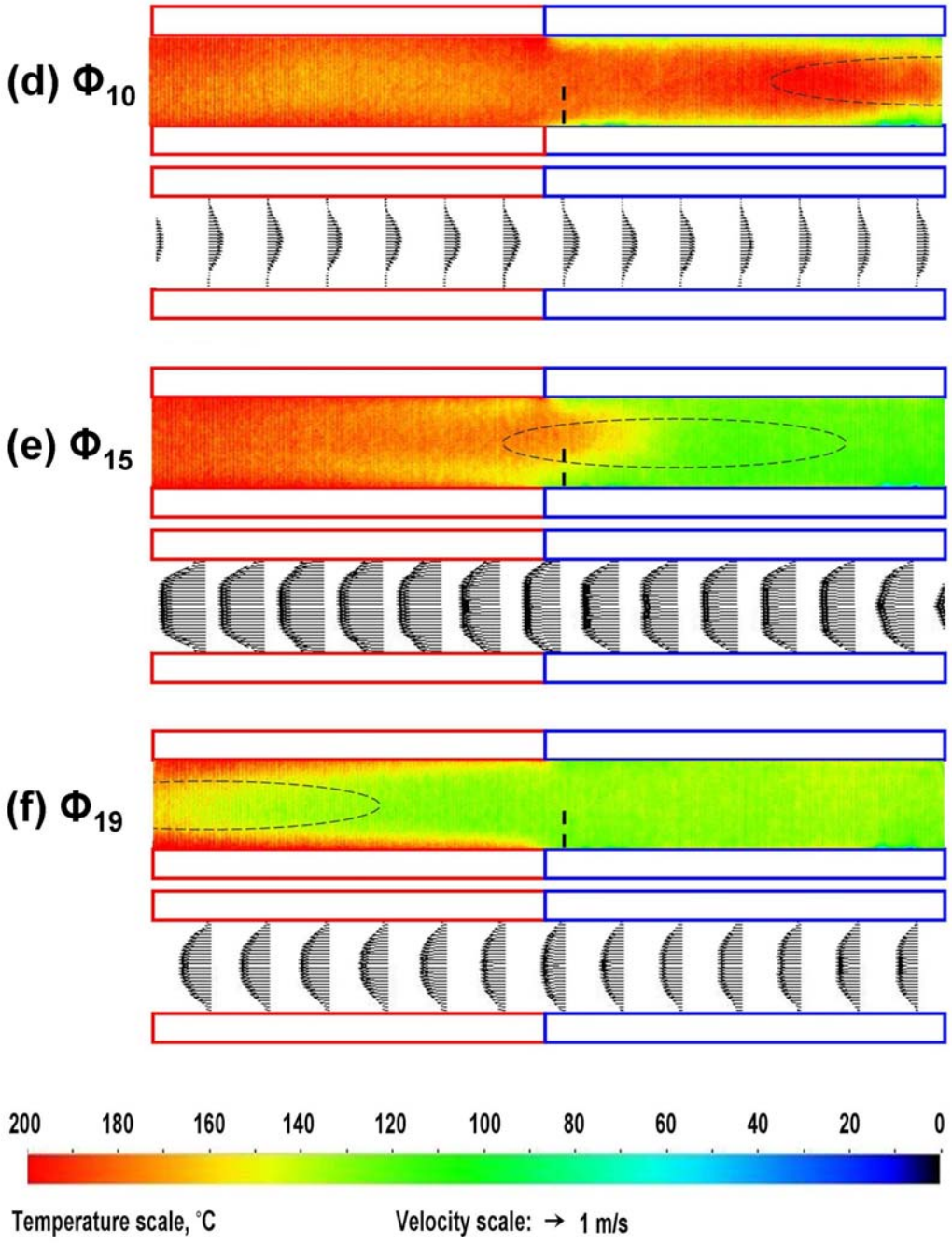

Figure 9 (*continued*) Temperature and velocity distributions for six selected phases in an acoustic cycle at drive ratio of 0.5%. Only one channel is shown, the viewing area being 6 x 53 mm. Red rectangles mark the heated plates, while blue rectangles mark the cooled plates in the heat exchanger assembly.

The temperature profiles in Figure 10a clearly show the heat transfer effects within the oscillating fluid. In a very thin layer of gas near to the wall, the temperature gradients are quite steep and indicate the heat transfer direction from the gas to the plate surface. This means that, for all of the six phases, the heat is transferred from the gas to the plate. As this heat has to pass this thin layer of gas via thermal conduction, the different slopes of the temperature gradient shown in Figure 10a indicate that the magnitudes of the heat flux are different for each phase.

Two concepts commonly used in thermoacoustic studies are the thermal and viscous penetration depths. These are defined as

$$\delta_\kappa = \sqrt{2\kappa/\omega}\,, \quad \delta_\nu = \sqrt{2\nu/\omega}\,, \tag{5}$$

respectively, where κ and ν are the thermal diffusivity and kinematic viscosity of gas, respectively, while ω is the angular frequency of acoustic excitation. These two characteristic lengths indicate how far heat and momentum can diffuse laterally during the time interval of the order of the period of the oscillation divided by 2π [2]. For example, for air at atmospheric pressure and oscillation frequency of 13.1 Hz, the thermal penetration depth at 303 K (30°C) is 0.746 mm, while it is 1.126 mm at 473 K (200°C). For the same pressure and frequency conditions, the viscous penetration depth is 0.627 mm at 303 K, and 0.921 mm at 473 K. It should be noted however that the flow situation described in this paper is not isothermal – and so for example the analytical solutions for the Stokes viscous layer would not apply, or in other words the thermal and viscous penetration depth would vary within the acoustic cycle if equations (5) were to be applied.

Turning back to Figure 10, the data presented seem to suggest certain interplay between the temperature and velocity fields. The temperature profiles for phase Φ_1, Φ_4 and Φ_7 exhibit an "overshoot" near the channel wall (strictly speaking the overshoot is not pronounced for Φ_1 yet, and is already very small for Φ_7, which is why phases Φ_2 and Φ_6 were added in Fig. 10a to prove the point). In some sense, this is similar to an already mentioned temperature "undershoot" seen in Figure 8e just to the left of the joint between the plates in phase Φ_{15}.

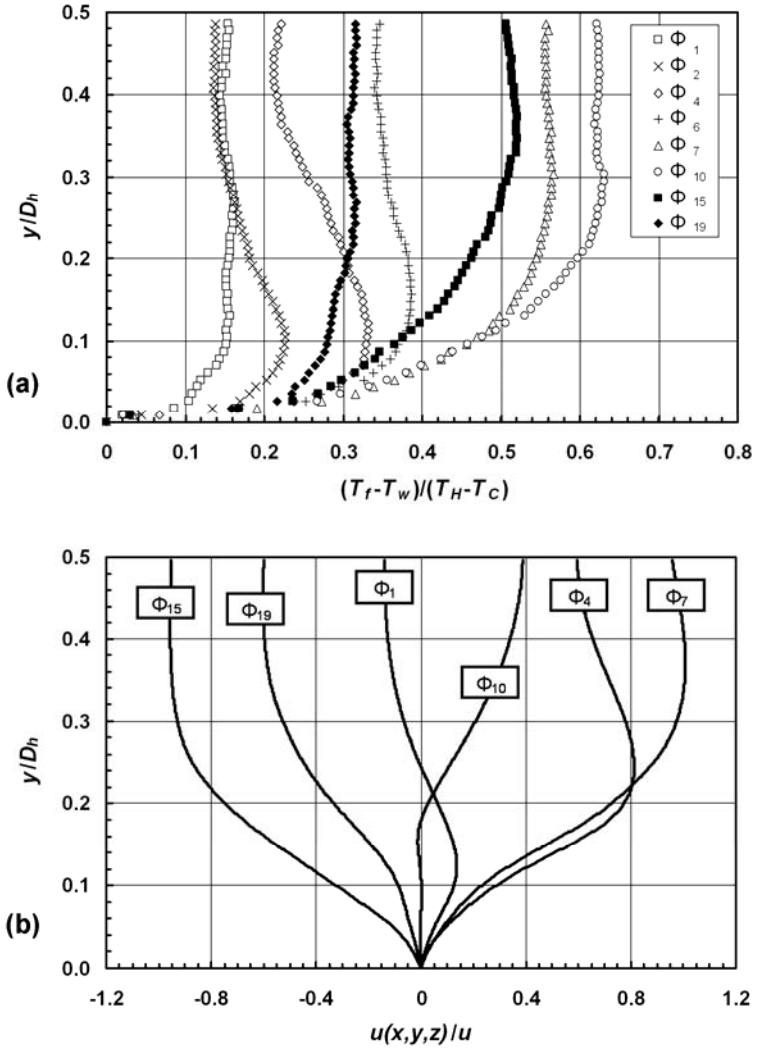

Figure 10 Normalised temperature distribution (a) and normalised axial velocity (b) within the half width of the channel at the position marked with a dashed line in Figure 9. Profiles are shown for the same six selected phases as in Figure 9. Drive ratio is 0.5%.

It is interesting to note that similar temperature "undershoot" (or "overshoot") effects have already been reported as part of numerical simulations by Zhao and Cheng [49, 50]. This concerned a numerical simulation of laminar forced convection in a heated pipe subjected to an oscillatory gas flow, which is somewhat similar to the experimental arrangement described in this paper. Their findings include an "annular effect" in the cross sectional temperature profiles near the entrance to the heated pipe, i.e. there is a temperature minimum near the wall, where the gas is colder than both the gas adjacent the wall and the gas close to the pipe centre. This is similar to the "temperature undershoot" pattern that was

highlighted when describing Figure 8e. They also found that the temperature annular effect became more pronounced when the kinetic Reynolds number (defined as $Re_\omega = \omega D^2/\upsilon$, where D is the pipe diameter) increases. Furthermore, the temperature annular effect did not exist far from the pipe entrance.

The temperature "undershoot" or "overshoot" effects (or the "annular effect" according to [49,50]) are most likely due to the combination of the velocity overshoot and the axial temperature gradient in the gas. From the Lagrangian point of view, the velocity overshoot must lead to a displacement overshoot, i.e., the gas parcel with velocity overshoot has a higher displacement than the gas near the wall and pipe centre. If there is an axial temperature gradient in the gas (such as the entrance to the heated pipe studied by Zhao and Cheng [49]), the gas parcel at the location of the displacement overshoot can either take the cold gas deeper into the pipe than other gas parcels, or take the hot gas farther out the heated pipe. As a result, from the Eulerian point of view, a local temperature minimum or maximum can be observed at the location where the velocity overshoot occurs, when viewing the cross sectional temperature profile. However, if there is no axial temperature gradient (such as in the pipe far from the entrance), although there is still a velocity overshoot and displacement overshoot, no temperature overshoot occurs. Following this explanation, it can be inferred that the temperature annular effect will be more pronounced when there is a stronger velocity overshoot or a steeper temperature gradient. In the actual fact, as shown above, Zhao and Cheng already found that the temperature annular effect was indeed more pronounced with the increase of the kinetic Reynolds number: a higher Reynolds number leads to a stronger velocity overshoot [50].

An analogous explanation should hold for the experimental data obtained in the current work: the cold channel is close to the hot channel and as a result, there is a steep axial temperature gradient in the gas near the joint. Therefore, in an oscillatory flow condition, the temperature "undershoot" (as shown in Figure 8 (e)) can be observed when the gas travels from the cold to the hot channel. Similarly, the temperature "overshoot" can be observed when the gas travels from the hot to the cold channel. Furthermore, one can find the temperature undershoot shown in Figure 9e is more pronounced than that shown in Figure 8e. This is because the kinetic Reynolds number of Figure 9e is higher than that in Figure 8e due to different drive ratio.

This type of unsteady effect on the wall temperature gradient may have a significant impact on the heat flux. In order to capture these effects a more detailed study would be required in the future where velocity and temperature fields would be studied in a smaller area with a higher temporal resolution – perhaps every degree or two for phases between $\Phi_{10} - \Phi_{15}$, instead of the standard 20 phases per full cycle. However this was somewhat outside the scope of the current study.

Finally, it is worthwhile to look more closely at the effect that imposing the temperature gradient has on the velocity field. Figure 11 shows the velocity profiles at the location marked by the dashed line in Figures 8 and 9, for all 20 investigated phases in the cycle, plotted for three cases: Figure 11a corresponds to the situation where there is no imposed temperature difference between the two heat exchangers, while the drive ratio is 0.3%. Figure 11b is for the case when there is a temperature gradient imposed and the drive ratio is 0.3%. Finally, Figure 11c is for the case when there is a temperature gradient imposed and the drive ratio is 0.5%.

When comparing Figures 11a and 11b, two effects are visible. Firstly, the shape of the velocity profiles seems to be "stretched" in the y-direction, as though the thickness of a hypothetical boundary layer was increased by a factor between 1.5 and 2. This may be to some extent explained by the fact that the viscosity is a function of temperature (comparing the viscous penetration depths between 293 and 473 K a factor of 1.5 seems reasonable – hotter fluid has a higher viscosity: hence according to equation (5) the viscous penetration depth increases). However relying on such explanation alone is overly simplistic. It needs to be remembered that while Fig. 11a represents a "cold" case, where both heat exchangers are at 20°C, Figs. 11b and 11c *do not* represent cases where both heat exchanger are at an elevated temperature (this would simply be not possible in the current arrangement). This is why, more interestingly, there are clearly some differences in the symmetry of the velocity profiles within the cycle in Figs. 11b and 11 c. For the situation with no temperature difference imposed, the velocity profiles for phase Φ_1 and Φ_{11} or Φ_7 and Φ_{17} are symmetrical with respect to the normal line to the plate surface (any small discrepancies can most likely be attributed to an asymmetrical location of the selected point). This is intuitively correct since for no temperature difference, flow directions "to the right" and "to the left" must have the same underlying physics. However, once the temperature gradient is present, the flow symmetry is broken: a

colder fluid flows from the right, while a hotter fluid flows from the left. The shapes of profiles Φ_1 vs. Φ_{11} or Φ_7 vs. Φ_{17} are clearly different. Therefore comparisons between Figs. 11a, b and c can only be qualitative at best, as a few different mechanisms interact simultaneously in the latter two cases. Firstly, the temperature varies within the cycle as the flow changes direction from left-to-right to right-to-left; secondly, there is no uniform temperature distribution across the channel; and thirdly there are complex thermal-viscous interactions in the "history" of the flow that affect the obtained instantaneous velocity profiles.

When comparing figures 11b and 11c (the difference being the drive ratio values) the main flow features are very similar – i.e. the lack of symmetry between the velocity profiles when the flow is "to the right" and "to the left". However, on closer inspection, some small differences can also be spotted. For example, when looking at (normalised) profiles for phase Φ_3 for the two cases, one can clearly see that one reaches the maximum value of around 0.66, while the other one is approximately 0.55. The underlying mechanism behind these differences must be related to the relative magnitude of the convective transport in the stream-wise direction and the conductive energy transfer in the span-wise direction.

5. Conclusions and future work

The combined measurement techniques of PIV and acetone-based PLIF have been developed to study the fluid flow and heat transfer processes in the oscillatory flow within a cold and hot heat exchanger setup, which mimics the physics of thermoacoustic processes. The velocity and temperature fields in one acoustic cycle at a relatively low Reynolds number have been illustrated. The time-dependent local gas velocity and temperature distributions normal to the heat exchanger fin at an arbitrarily selected position have been discussed to illustrate the potential of the developed measurement methods to study the interplay between thermal, viscous and inertial effects.

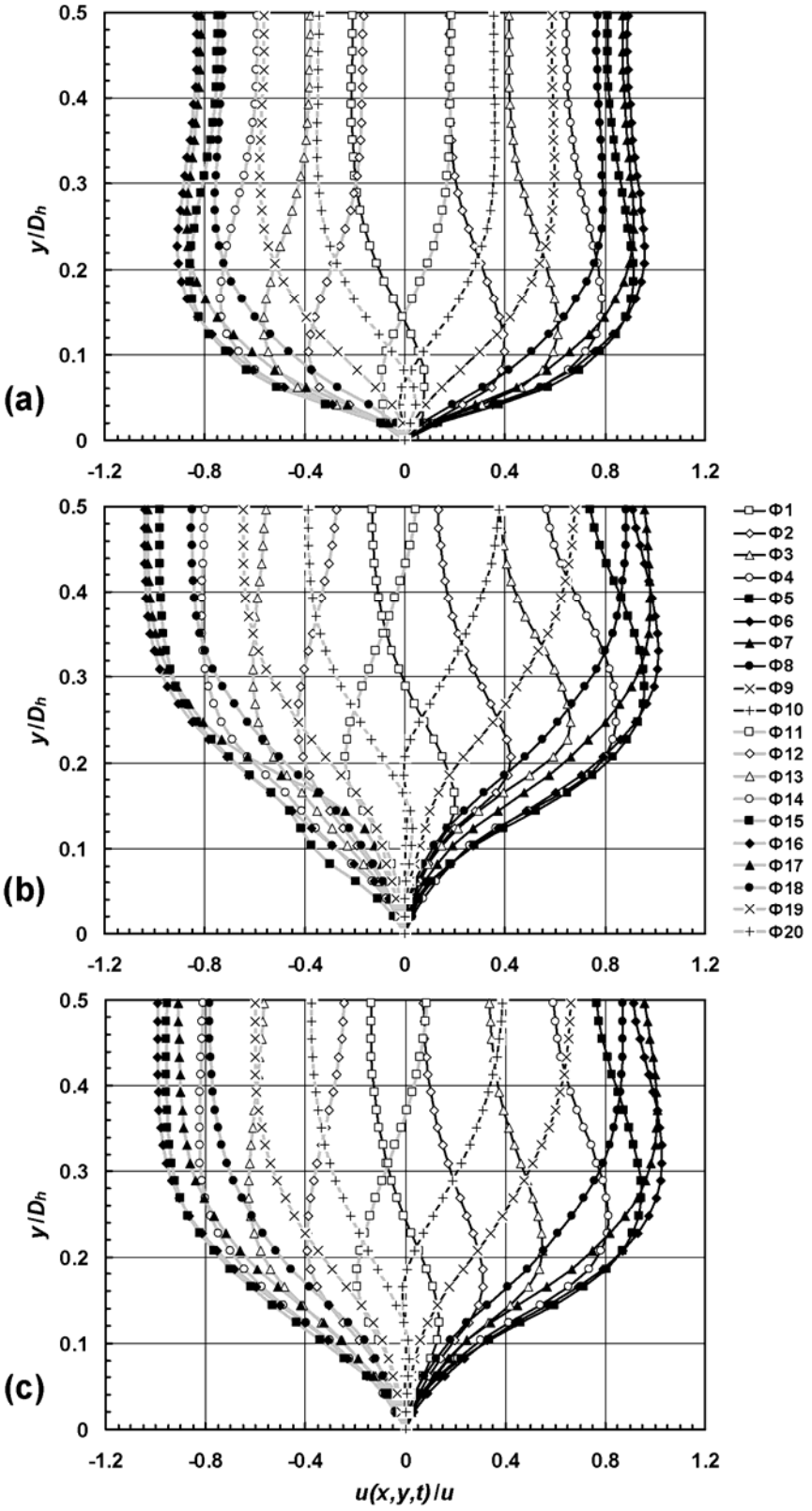

Figure 11 Velocity distributions for three cases: (a) no temperature gradient, drive ratio 0.3%; (b) temperature gradient present, drive ratio 0.3%; (c) temperature gradient present, drive ratio 0.5%.

The measurements showed an overshoot in velocity and temperature distributions. The overshoot in the velocity distribution is due to the viscous and inertial effect in the gas, while the overshoot in temperature distribution is most likely due to the velocity overshooting and the combined effect of the viscous and thermal boundary layers. Similarly, the velocity boundary layer thickness is strongly affected by the gas temperature change, which causes the change of gas viscosity. These results indicate that in thermoacoustic systems there is a strong interaction between the velocity and temperature fields. Furthermore it was shown that there is an asymmetry in the velocity profiles caused by the imposed longitudinal temperature gradient.

However the methodologies and experimental techniques developed during the course of this work have potentially much wider implications for studying thermoacoustic, or more generally oscillatory, heat transfer processes. In particular it seems feasible to directly derive absolute values of heat transfer rates. For example, experimental data such as presented in Figure 10a allow calculations of local, phase-dependent, heat fluxes on the heat exchanger surface using first principles:

$$q(x,\phi) = -k\left.\frac{dT(x,y,\phi)}{dy}\right|_{y=0} \tag{6}$$

where k is the gas thermal conductivity, the normal temperature gradient calculated from the slope of the temperature distributions.

Clearly, calculations of the local heat transfer rates along the plate surface and a subsequent surface integration could lead to obtaining the total phase dependent (instantaneous) heat transfer rates, while further integration over the acoustic cycle would lead to total cycle-averaged values. Obtaining both instantaneous and cycle-averaged total heat transfer rates would allow formulating non-dimensional equations for phase-dependent and cycle averaged Nusselt numbers as a function of flow conditions, heat exchanger geometry and fluid parameters. However studying the feasibility of such approach requires further research.

Following preliminary results reported in this paper, future work will focus on the following aspects: (i) Development of alternative tracer techniques for PLIF. This will in particular include studies with toluene vapour, which should potentially offer higher temperature resolution, higher accuracy and simplified or no calibration procedures. (ii) Development of further rig capabilities, in particular to handle helium as the working gas. (iii) Improvements of the optical access and laser illumination, in particular to remove the fin mounting "pillars" from the field of view and to apply beam splitters and/or additional mirrors to enable illumination of the gap between hot and cold heat exchangers. (iv) Design and fabrication of alternative heat exchanger configurations, in particular different thickness and length, to enable non-dimensional studies of heat transfer processes. (v) Development of data processing procedures, in particular to calculate local and total heat transfer rates, both instantaneous and cycle averaged. (vi) Non-dimensional studies to derive appropriate Nusselt number correlations to describe heat transfer processes in oscillatory flows. (vii) Further hardware development to enable capturing simultaneous time-dependent temperature and velocity fields in order to calculate the temperature and velocity fluctuation cross-products $\langle u'T' \rangle$ and $\langle v'T' \rangle$ and thus deduce the nature of hydrodynamic energy fluxes.

Acknowledgments:

The authors wish to thank the Engineering and Physical Sciences Research Council UK for supporting this work under grants: GR/S26842/01, GR/T04502/01 (EPSRC Advanced Research Fellowship), GR/T04519/01 and EP/E044379/1 and the European Commission for funding under grant THATEA, reference number 226415.

List of References:

[1] Rayleigh, L., *The Theory of Sound, 1894*, Dover Publications, New York, 1945.

[2] Swift, G.W., "Thermoacoustic Engines". *Journal of the Acoustical Society of America*, Vol. 84, 1988, pp. 1145-1180.

[3] Mao, X., Yu, Z., and Jaworski, A. J., "PIV Studies of Coherent Structures Generated at the End of a Stack of Parallel Plates in a Standing Wave Acoustic Field," *Experiments in Fluids*, Vol, 45, pp. 833-846, 2008.

[4] Leong K.C., and Jin, L.W., "An experimental study of heat transfer in oscillating flow through a channel filled with an aluminum foam", *International Journal of Heat and Mass Transfer*, Vol. 48, 2005, pp. 243–253

[5] Leong K.C., and Jin, L.W., "Effect of oscillatory frequency on heat transfer in metal foam heat sinks of various pore densities", *International Journal of Heat and Mass Transfer*, Vol. 49, 2006, pp. 671–681.

[6] Jin, L.W., and Leong K.C., "Heat Transfer Performance of Metal Foam Heat Sinks Subjected to Oscillating Flow", *IEEE Transactions on Components and Packaging Technologies*, Vol. 29, No. 4, 2006, pp. 856-863.

[7] Gopinath, A., and Harder, D.R., "An Experimental Study of Heat Transfer from a Cylinder in Low-Amplitude Zero-Mean Oscillatory Flows," *International Journal of Heat and Mass Transfer*, Vol. 43, No. 4, 2000, pp. 505-520.

[8] Paek I, Braun J.E., and Mongeau L., "Characterizing heat transfer coefficients for heat exchangers in standing wave thermoacoustic coolers", *Journal of the Acoustical Society of America*, Vol. 118, No. 4, 2005, pp. 2271-2280.

[9] Nsofor, E.C., Celik, S., and Wang, X., "Experimental Study on the Heat Transfer at the Heat Exchanger of the Thermoacoustic Refrigerating System," *Applied Thermal Engineering*, Vol. 27, No. 14-15, 2007, pp. 2435-2442.

[10] Huelsz, G., and Ramos, E., "Temperature Measurements inside the Oscillatory Boundary Layer Produced by Acoustic Waves," *The Journal of the Acoustical Society of America*, Vol. 103, 1998, pp. 1532.

[11] Mao, X., and Jaworski, A.J., "Measurement of Boundary Layer in a Channel of Parallel-Plate Thermoacoustic Stack," *Proc. 22nd International Congress of Refrigeration*, Beijing, China, 21 August 2007 (paper ICR07-A1-275).

[12] Wetzel, M., Herman, C., "Accurate measurement of high-speed, unsteady temperature fields by holographic interferometry in the presence of periodic pressure variations", *Measurement Science and Technology*, Vol. 9, 1998, pp. 939-951

[13] Wetzel, M., Herman, C., "Experimental study of thermoacoustic effects on a single plate part II: heat transfer", *Heat and Mass Transfer*, Vol. 35, No. 6, 1999, pp. 433-441.

[14] Wetzel, M., Herman, C., "Experimental study of thermoacoustic effects on a single plate part I: temperature fields", *Heat and Mass Transfer*, Vol. 36, No. 1, 2000, p. 7-20.

[15] Huelsz, G., and Lopez-Alquicira, F., "Hot-wire anemometry in acoustic waves", *Experiments in Fluids*, Vol. 30, 2001, pp. 283-285.

[16] Mao, X.A., Jaworski A.J., and Shi L., "The boundary layer velocity measurements in a high-amplitude standing wave thermoacoustic stack", *Proc. 22nd IIR International Congress of Refrigeration*, Beijing (paper ICR07-A1-281), 21 August 2007.

[17] Bailliet, H., Lotton, P., Bruneau, M., Gusiev, V., Valiere, J.C., and Gazengel, B., "Acoustic Power flow measurement in a thermoacoustic resonator by means of laser Doppler anemometry (L.D.A.) and microphonic measurement", *Applied Acoustics*, Vol. 60, 2000, pp. 1-11.

[18] Thompson, M.W., Atchley, A.A., and Maccarone. M.J., "Influence of a temperature gradient and fluid inertia on acoustic streaming in a standing wave", *Journal of the Acoustical Society of America*, Vol. 117, No. 4, pp. 1839-1849.

[19] Hann, D.B., and Greated, C.A., "Particle image velocimetry for the measurement of mean and acoustic particle velocities", *Meas. Sci. Technol.*, Vol. 8, 1997, pp. 656-660.

[20] Hann, D.B., and Greated, C.A., "The measurement of flow velocity and acoustic particle velocity using particle-image velocimetry", *Meas. Sci. Technol.*, Vol. 8, 1997, pp. 1517-1522.

[21] Campbell, M., Cosgrove, J.A., Greated, C.A., Jack, S., and Rockliff, D., "Review of LDA and PIV applied to the measurement of sound and acoustic streaming", *Optics and Laser Technology*, Vol. 32, 2000, pp. 629-639.

[22] Nabavi, M., Siddiqui, M.H.K., and Dargahi, J., "Simultaneous measurement of acoustic and streaming velocities using synchronized PIV technique", *Meas. Sci. Technol.*, Vol. 18, 2007, pp. 1811–1817.

[23] Debesse, Ph., Baltean-Carlès, D., Lusseyran, F., and François M.-X., "Experimental analysis of nonlinear phenomena in a thermoacoustic system", *AIP Conference Proceedings*, Vol. 1022, 2008, pp. 355-358.

[24] Blanc-Benon, P., Besnoin, E., and Knio, O. M., "Experimental and computational visualization of the flow in a thermoacoustic stack", *C R. Mécanique*, Vol. 331, 2003, pp. 17-24.

[25] Castrejón-Pita, J.R., Castrejón-Pita, A.A., Huelsz, G., and Tovar, R., "Experimental demonstration of the Rayleigh acoustic viscous boundary layer theory", *Physical Review E*, Vol. 73, No. 3, 2006, pp. 036601.

[26] Mao, X., Marx, D., and Jaworski, A.J., "PIV Measurement of Coherent Structures and Turbulence Created by an Oscillating Flow at the End of a Thermoacoustic Stack" in "Progress in Turbulence II", ed. Oberlack M et al, *Springer Proceedings in Physics*, Vol. 109, 2007, pp. 99-102

[27] Berson, A., and Blanc-Benon, Ph., "Nonperiodicity of the flow within the gap of a thermoacoustic couple at high amplitudes", *J. Acoust. Soc. Am.*, Vol. 122, No. 4, 2007, pp. EL122-EL127.

[28] Berson, A., Michard, M., and Blanc-Benon, Ph., "Measurement of acoustic velocity in the stack of a thermoacoustic refrigerator using particle image velocimetry", *Heat Mass Transfer*, Vol. 44, 2008, pp. 1015-1023.

[29] Aben, P.C.H., Bloemen, P.R., and Zeegers, J.C.H., "2-D PIV measurements of oscillatory flow around parallel plates", *Exp. Fluids*, Vol. 46, 2009, pp. 631–641.

[30] Jaworski, A.J., Mao, X., Mao, X., and Yu, Z., "Entrance effects in the channels of the parallel plate stack in oscillatory flow conditions", *Experimental Thermal and Fluid Science*, Vol. 33, 2009, pp. 495–502.

[31] Bresson, A., Brossard, C., Gicquel, P., and Grisch, F., "Simultaneous Temperature, Concentration, and Velocity Fields Measurements in a Turbulent Heated Jet Using Combined Laser-Induced Fluorescence and PIV," *SPIE*, 2003.

[32] Lozano, A., Yip B., and Hanson R.K., "Acetone: a tracer for concentration measurements in gaseous flows by planar laser-induced fluorescence", *Experiments in Fluids*, Vol. 13, No.6, 1992, pp. 369-376.

[33] Thurber, M.C., Grisch, F., Kirby, B. J., Votsmeier, M., and Hanson, R.K., "Measurements and Modeling of Acetone Laser-induced Fluorescence with Implications for Temperature-imaging Diagnostics," *Applied Optics,* Vol. 37, No, 21, 1998.

[34] Thurber, M.C., "Acetone Laser-Induced Fluorescence for Temperature and Multiparameter Imaging in Gaseous Flows," Thermophysics Division, Department of Mechanical Engineering, PhD Thesis, Stanford University, Stanford, California, 1999.

[35] Meyer, T.R., Dutton J.C., and Lucht R.P., "Vortex interaction and mixing in a driven gaseous axisymmetric jet", *Physics of Fluids*, Vol. 11, 1999, p. 3401.

[36] Webster, D. R., Roberts, P. J. W., Raad, L., "Simultaneous DPTV PLIF measurements of a turbulent jet", *Experiments in Fluids*, Vol. 30, 2001, pp. 65-72.

[37] Kearney, S.P., and Reyes, F.V., "Quantitative Temperature Imaging in Gas-phase Turbulent Thermal Convection by Laser-induced Fluorescence of Acetone," *Experiments in Fluids*, Vol. 34, No. 1, pp. 87-97, 2003.

[38] LaVision Product-Manual, 2007.

[39] Marx, D., Mao, X., and Jaworski A.J., "Acoustic coupling between the loudspeaker and the resonator in a standing-wave thermoacoustic device", *Applied Acoustics*, Vol. 67, No. 5, pp. 402-419.

[40] Wakeland, R.S., and Keolian, R.M., "Thermoacoustics with idealized heat exchangers and no stack", *Journal of the Acoustical Society of America*, Vol. 111, No. 6, 2002, pp. 2654-2664.

[41] Wakeland, R.S., and Keolian, R.M., "Calculated effects of pressure-driven temperature oscillations on heat exchangers in thermoacoustic devices with and without a stack" , *Journal of the Acoustical Society of America*, Vol. 116, No. 1, 2004, pp. 294-302.

[42] Merkli, P., and Thomann, H., "Transition to Turbulence in Oscillating Pipe Flow," *Journal of Fluid Mechanics*, Vol. 68, No. 3, pp. 567-575, 1975.

[43] Kurzweg, U.H., Lindgren, E.R., and Lothrop B., "Onset of turbulence in oscillating flow at low Womersley number", *Physics of Fluids A*, Vol. 1, No. 12, 1989, pp. 1972-1975.

[44] Adrian, R.J., "Dynamic Ranges of Velocity and Spatial Resolution of Particle Image Velocimetry," *Measurement Science and Technology*, Vol. 8, No. 12, 1997, pp. 1393-1398.

[45] Swift, G.W., *Thermoacoustics: A unifying perspective for some engines and refrigerators*, Acoustical Society of America, New York, 2002.

[46] Mao X. and Jaworski A.J., "Application of particle image velocimetry measurement techniques to study turbulence characteristics of oscillatory flows around parallel-plate structures in thermoacoustic devices," *Measurement Science and Technology*, Vol. 21(3), 2010, 035403 (16p.).

[47] Shi, L., Yu, Z., and Jaworski A. J., "PLIF Measurement of instantaneous temperature field within thermoacoustic heat exchangers", *Proc. 2009 SEM Annual Conference and Exposition on Experimental and Applied Mechanics*, Albuquerque, New Mexico, USA, June 1-4, 2009.

[48] Shi, L., Yu, Z., and Jaworski A. J., "Development of Experimental Methods to Capture the Unsteady Temperature Field Distributions in Thermoacoustic Devices", *Experimental Techniques*, in press.

[49] Zhao, T., and Cheng, P., "A numerical solution of laminar forced convection in a heated pipe subjected to a reciprocating flow", *International Journal of Heat and Mass Transfer*, Vol. 38, No. 16, 1995, pp. 3011-3022.

[50] Zhao, T. and Cheng, P., "Heat transfer in oscillatory flows", Annual Review of Heat Transfer, Vol. IX, 1998.

List of symbols

A,	local Reynolds number, [-]
D_h,	gap between the heat exchanger fins, [m]
d_h,	thickness of the heat exchanger fin, [m]
k,	thermal conductivity, [W m^{-1} K^{-1}]
l_h,	length of the heat exchanger fin, [m]
Re,	regular Reynolds number, [-]
T_C,	reference cold heat exchanger temperature, [K]
T_f,	instantaneous local fluid temperature, [K]
T_H,	reference hot heat exchanger temperature, [K]
T_w,	local wall temperature, [K]
u,	velocity amplitude within the heat exchanger, [m s^{-1}]
$u(x,y,t)$,	instantaneous local fluid velocity, [m s^{-1}]
Wo	Womersley number, [-]
δ_κ,	thermal penetration depth, [m]
δ_ν,	viscous penetration depth [m]
ξ,	displacement amplitude of gas particle, [m]
θ,	normalised fluid temperature, [-]
κ,	thermal diffusivity, [m^2 s^{-1}]
ν,	kinematic viscosity, [m^2 s^{-1}]
ϕ,	tested phase in an acoustic cycle, [°]
ω,	oscillation angular frequency [rad s^{-1}]